Using thermo-mechanical models of subduction to constrain effective mantle viscosity

Fanny Garel, Catherine Thoraval, Andrea Tommasi, Sylvie Demouchy, D. Rhodri Davies

▶ **To cite this version:**

HAL Id: hal-02733023

https://hal.umontpellier.fr/hal-02733023

Submitted on 14 Jul 2020

Using thermo-mechanical models of subduction to constrain effective mantle viscosity

Fanny Garel [a,*], Catherine Thoraval [a], Andréa Tommasi [a], Sylvie Demouchy [a],
D. Rhodri Davies [b]

[a] *Géosciences Montpellier, Univ. Montpellier, CNRS, Montpellier, France*
[b] *Research School of Earth Sciences, The Australian National University, Canberra, Australia*

ABSTRACT

Mantle convection and plate dynamics transfer and deform solid material on scales of hundreds to thousands of km. However, viscoplastic deformation of rocks arises from motions of defects at sub-crystal scale, such as vacancies or dislocations. In this study, results from numerical experiments of dislocation dynamics in olivine for temperatures and stresses relevant for both lithospheric and asthenospheric mantle (800–1700 K and 50–500 MPa; Gouriet et al., 2019) are used to derive three sigmoid parameterizations (*erf, tanh, algebraic*), which express stress evolution as a function of temperature and strain rate. The three parameterizations fit well the results of dislocation dynamics models and may be easily incorporated into geodynamical models. Here, they are used in an upper mantle thermo-mechanical model of subduction, in association with diffusion creep and pseudo-brittle flow laws. Simulations using different dislocation creep parameterizations exhibit distinct dynamics, from unrealistically fast-sinking slabs in the *erf* case to very slowly-sinking slabs in the *algebraic* case. These differences could not have been predicted a priori from comparison with experimentally determined mechanical data, since they principally arise from feedbacks between slab sinking velocity, temperature, drag, and buoyancy, which are controlled by the strain rate dependence of the effective asthenosphere viscosity. Comparison of model predictions to geophysical observations and to upper-mantle viscosity inferred from glacial isostatic adjustment shows that the *tanh* parameterization best fits both crystal-scale and Earth-scale constraints. However, the parameterization of diffusion creep is also important for subduction bulk dynamics since it sets the viscosity of slowly deforming domains in the convecting mantle. Within the range of uncertainties of experimental data and, most importantly, of the actual rheological parameters prevailing in the upper mantle (e.g. grain size, chemistry), viscosity enabling realistic mantle properties and plate dynamics may be reproduced by several combinations of parameterizations for different deformation mechanisms. Deriving mantle rheology cannot therefore rely solely on the extrapolation of semi-empirical flow laws. The present study shows that thermo-mechanical models of plate and mantle dynamics can be used to constrain the effective rheology of Earth's mantle in the presence of multiple deformation mechanisms.

1. Introduction

Mantle and lithosphere dynamics is a multi-scale process, in which the motion of defects at a sub-crystal scale induces deformation at scales exceeding thousands of kilometers. Earth's lithosphere deforms elastically at short time-scales, from milliseconds for seismic stress release (e.g. Melosh and Fleitout, 1982) to several thousand years of glacial loading and unloading (e.g. Watts,

2001). Earthquake distribution in oceanic plates away from subduction zones indicates that brittle failure is active at low pressure and temperature conditions (<1 GPa, <600 K; McKenzie et al., 2005). On the time-scales of million years, viscous deformation over hundreds of kilometers is revealed by seismic tomography images showing deformed subducted slabs in the deep mantle (e.g. Kárason and Van Der Hilst, 2000). This deformation is essentially accommodated by viscoplastic processes allowing the flow of mantle rocks at high pressure.

Laboratory experiments have long investigated the deformation of olivine, the most abundant upper mantle mineral (~60% in volume), to constrain its rheological properties, i.e. how it deforms
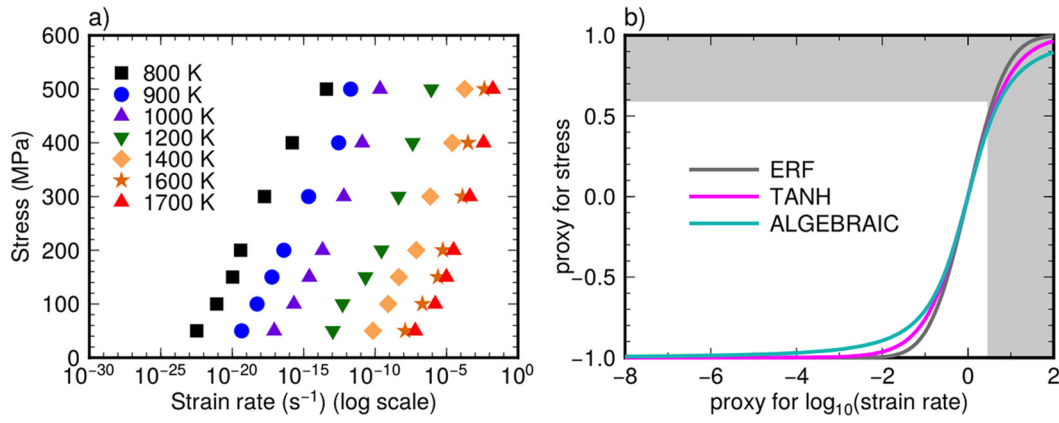
Fig. 1. a) Results from dislocation dynamics simulations (Gouriet et al., 2019) with stress as a function of strain rate for temperatures ranging from 800 to 1700 K. b) Sigmoid functions (*erf, tanh, algebraic*) used as fitting functions. They reproduce both the rapid increase at high strain rates and the asymptotic behavior towards zero at low stresses and low strain rates. The data set is restrained to stresses lower or equal to 500 MPa. Given the shape of a sigmoid function, the parameterizations should not be extrapolated at high strain rate and high stresses (shaded domain on Fig. 1b). (For interpretation of the colors in the figure(s), the reader is referred to the web version of this article.)

under an applied stress. At high temperatures, ductile deformation through creep processes predominates. These processes involve the motion of crystal defects. At high stresses or strain rates, the motion of line defects across the crystal predominates, characterizing the dislocation creep regime (see review by Ashby and Verrall, 1978; Hirth and Kohlstedt, 2003). At lower stresses and higher temperatures, the diffusion of point defects – vacancies – plays a major role. This diffusion creep regime is grain-size sensitive. Experimental data for dislocation creep in olivine point to a variation in mechanical behavior as a function of stress and/or temperature. The high-temperature data are classically adjusted using a semi-empirical flow law in which strain rates depend on stress to a power n (power-law rheology; Bai et al., 1991; Hirth and Kohlstedt, 2003), whereas the low-temperature data is better described by a rheological parameterization in which strain rates depend exponentially on stress (e.g. Evans and Goetze, 1979; Demouchy et al., 2013).

Nevertheless, extrapolation of experimentally determined flow laws to nature is hindered by the fact that the strain rate range in the deformation experiments ($>10^{-6}$ s^{-1}) is at least 6 orders of magnitude faster than the strain rates expected in the convecting mantle ($\sim 10^{-20}$–10^{-12} s^{-1}). Moreover, steady state is never achieved in the low temperatures experiments (Demouchy et al., 2013; Thieme et al., 2018). Recently, the increased efficiency of numerical calculus allowed the development of numerical simulations in which the dislocation dynamics in olivine, including both glide and climb, is explicitly modeled (Boioli et al., 2015). For the first time, these models calculated the interactions between dislocation glide and climb in olivine at both laboratory and geological strain rates, avoiding extrapolation of the empirically-determined parameters. Recently, Gouriet et al. (2019) continued this task, establishing that the change in mechanical behavior associated with the "power-law breakdown", which in these models occurs for applied stresses greater than 150 MPa, especially at low temperatures, is not due to a change from a climb-controlled to a glide-controlled creep. They showed a continuity of dynamical processes. Strain is produced almost entirely by glide, but strain rates are controlled by climb. Variations in stress and temperature within a range relevant for both the lithospheric and the asthenospheric mantle (50–500 MPa and 800–1700 K) continuously impact the interactions between climb and glide. The mechanical behavior can then be described by a unified semi-empirical flow law (Gouriet et al., 2019).

Constitutive equations of rocks rheology derived from deformation experiments usually express the strain rate as a function of the applied stress. However, it is often more convenient in nu-

merical models of geodynamics to express stress as a function of strain rate and temperature. The flow laws implemented in these models are parameterizations, partly based on deformation and diffusion experiments on minerals and rocks. The constants in these equations (e.g. activation volumes and energies) are either derived directly from experimental data (e.g. van Hunen et al., 2000; Crameri and Kaus, 2010) or are assigned *ad hoc* values (e.g. Tackley, 1996). However, even in the first case, there are uncertainties in the actual values of most rheological parameters in the mantle (pre-exponential constant, activation volume and energy for both dislocation and diffusion creep) as well as in other important parameters, such as grain size, hydrogen concentration, oxygen fugacity, etc. Moreover, numerical models implicitly extrapolate the crystal- or polycrystal rheological properties to the scale of model spatial resolution (usually larger than several hundreds of meters, e.g. Davies et al., 2011).

In this study, we derive several parameterizations based on the results of the dislocation dynamics simulations, in addition to the first one proposed in Gouriet et al. (2019) and implement these dislocation creep parameterizations, along with classical flow laws for diffusion creep and pseudo-brittle yielding, in a thermo-mechanical model of upper mantle subduction. We analyze the effects of the rheological parameterizations on the feedbacks between slab sinking velocity, temperature, drag, and buoyancy and compare the subduction dynamics predicted by the different simulations to observational constraints on large-scale mantle dynamics. This approach, which is complementary to inversion of rheological parameters from surface observations (e.g. Baumann and Kaus, 2015), shows how thermo-mechanical models of plate and mantle dynamics may further help constraining mantle rheology.

2. Methods

2.1. Parameterizing dislocation creep in olivine

We search for a mathematical formulation expressing stress solely as a function of strain rate and temperature and ensuring mechanical consistency (strain rates should tend to zero when stress tends to zero). The parameterization should fit the most recent numerical deformation simulations for forsterite single crystals obtained from dislocation dynamics models (Gouriet et al., 2019). The data set, shown in Fig. 1a, corresponds to 49 strain rate values obtained from 150 numerical simulations performed at ambient pressure, for seven fixed applied differential stresses (i.e. the difference between maximal and minimal applied stress) between 50 and 500 MPa (uniaxial loading) and for seven temperatures be-
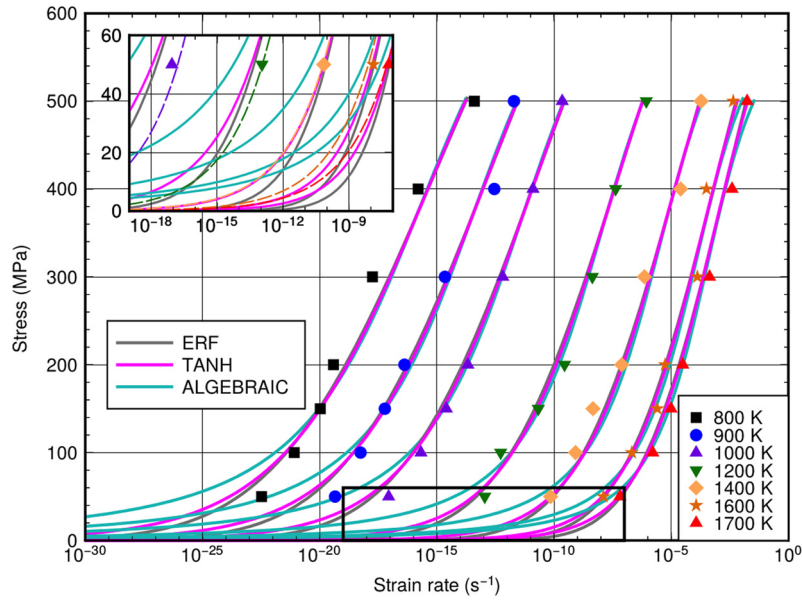
Fig. 2. The three sigmoid functions (Eq. (1) and (2)) with coefficients from Table S1 (Supplementary Material) are displayed for the seven temperatures corresponding to the results of dislocation-dynamics calculations (Gouriet et al., 2019, colored markers as in Fig. 1) in a differential stress σ_d vs. uniaxial strain rate $\dot{\varepsilon}$ graph. The insert shows a zoom at high temperatures and high strain rates, in a range relevant for a deforming asthenospheric mantle, with dashed curves displaying the power-law fit (Eq. (3)) for the five highest temperatures and with parameters from Gouriet et al. (2019), see section 2.1 for details.

tween 800 K and 1700 K. The shape of the mathematical functions used for the parameterization is constrained by: (i) an asymptotic behavior towards zero stress at zero strain rate; and (ii) the rapid increase of stress above a critical strain rate shown by the results from Gouriet et al. (2019), the latter being steeper as temperature increases. Sigmoid functions meet these criteria. We choose three different sigmoid functions: the error function *erf* (already presented in Gouriet et al., 2019), the hyperbolic tangent function *tanh*, and an *algebraic* function $f(x) = (x/\sqrt{1 + x^2})$. They range from −1 to 1, are symmetrical relative to 0, and differ only at the transition between the asymptotic part and the steep increase, as they exhibit distinct curvatures (Fig. 1b).

Differential stress σ_d at each temperature is expressed as a function of strain rate $\dot{\varepsilon}$ (shortening parallel to the direction of the applied compression), following

$$\sigma_d = A_0\left[1 + SF\left[A_1\left(\log_{10}(\dot{\varepsilon}) - A_2\right)\right]\right] \qquad (1)$$

with *SF* the sigmoid function, and A_0, A_1, A_2 being three coefficients dependent on temperature. The formulation of Eq. (1) shifts the asymptotic limit to 0 as required. In a first step, the three coefficients A_0, A_1, A_2 are calculated independently to best match the data at each temperature using a nonlinear least-squares solver using a trust-region-reflective algorithm based on the interior-reflective Newton method (here the "lsqcurvefit" MATLAB solver). In a second step, the temperature-dependence of each coefficient is expressed as a first-order (A_0, A_1) or second-order (A_2) polynomial function in order to best fit the temperature-dependency of deformation:

$$A_0(T) = a_0 + b_0 T$$
$$A_1(T) = a_1 + b_1 T \qquad (2)$$
$$A_2(T) = a_2 + b_2 T + c_2 T^2$$

with T the temperature in K.

Finally, the seven polynomial coefficients a_0, b_0, a_1, b_1, a_2, b_2, c_2 are determined for the whole data set simultaneously with the "lsqcurvefit" MATLAB solver (with initial guesses from the fitted

polynomial functions, followed by iterative least-squared fits). Additional tests have been performed to ensure the robustness of the solution when excluding either the highest or the lowest temperature data.

Stress variation as a function of strain rate and temperature is fully described by the seven coefficients in Eq. (2). The best fitting coefficients (see Fig. 2) for the three different sigmoid functions (more than 98% of variance explained for all three parameterizations) are given in Supplementary Material Table S1. For stresses ranging from 150–500 MPa, which correspond to the steepest part of the curves, the three parameterizations are almost exactly superimposed. On the other hand, at stresses below 150 MPa, the curves, and hence the predictions of the three parameterizations, differ as a consequence of the different curvatures (Fig. 1b). For instance, the stress predicted for a strain rate of 10^{-15} s^{-1} at 1400 K is 1, 4, and 18 MPa for the *erf*, *tanh* and *algebraic* parameterizations, respectively. The experimental data at 50 MPa are better adjusted by the *erf* and *tanh* parameterizations. The fit for all three parameterizations becomes poorer as both stress and temperature decrease, in particular below 150 MPa and 1100 K. Yet, the conditions at which the fit is degraded are associated with very slow strain rates ($<10^{-16}$ s^{-1}). Note that the parameterizations are not constrained by DD simulations at stresses higher than 500 MPa: using them beyond this value is an extrapolation.

The unified creep parameterization of Eq. (1) is a continuous function of temperature and strain rate, applicable for dislocation creep at both low and high temperatures. It is a useful alternative to the double parameterization of plasticity depending on the temperature or stress range, which have been used in previous geodynamical models (e.g. Neves et al., 2008).

For comparison, the curves corresponding to a "classical", high-temperature power-law parameterization for dislocation creep

$$\dot{\varepsilon} = A_{PL}\sigma_d{}^n \exp\left(-\frac{E_{disl}}{RT}\right) \qquad (3)$$

with pre-exponential factor $A_{PL} = 5.27\ 10^{-29}$ Pa^{-n}.s^{-1}, $n = 4.5$, and activation energy $E_{disl} = 443$ kJ.mol^{-1} (Gouriet et al., 2019) are shown in the insert of Fig. 2. The expression of Eq. (3) also predicts an asymptotic behavior towards null strain rates at null stresses
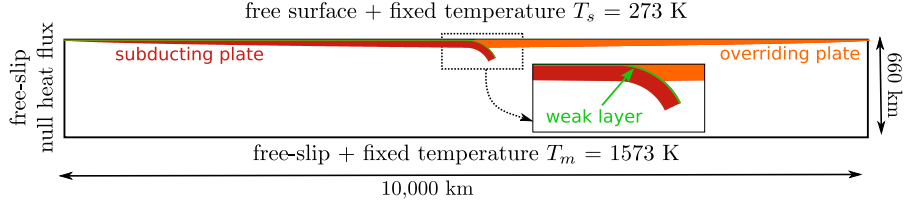
Fig. 3. Subduction model set-up ($10,000 \times 660$ km box). The initial ages of the subducting and overriding plates at the trench are 40 Myr (see additional thermal and density profiles in Supplementary Fig. S1). The weak layer is 7.5-km thick. The initial slab tip depth is 194 km, and the initial slab width is 96 km. See text for further details on material properties.

and fits well the dislocation dynamics data at stresses lower than 150 MPa. The *tanh* parameterization is the closest to the power law one at stresses below 50 MPa. Since the dislocation dynamic simulations were performed at ambient pressure, Eq. (1) does not feature any pressure-dependency, nor does Eq. (3), e.g. there is no activation volume. Depth-dependency of rheological flow laws arises from the increase of both pressure and temperature with depth, which are expected to at least partly compensate each other (see more details in sections 2.3 and 4.3). Hence, potential temperatures T are used in Eq. (1) to calculate rheology for the whole mantle domain in our simulations at mantle pressures.

2.2. Set-up of subduction model

The three parameterizations for dislocation creep in olivine (Eq. (1)–(2)) are implemented in a 2-D numerical thermo-mechanical model of subduction to quantify how they influence the dynamics in a subduction setting. The model geometry follows Garel et al. (2014), with cold subducting and overriding plates at the top of a 660-km deep (i.e. restricted to the upper mantle) and 10,000-km wide domain (Fig. 3). The trench corresponds to the interface between the two plates and is free to move in response to their dynamics. It is initially located in the middle of the domain (X = 5,000 km). The initial plate ages are zero at the left and right corner ridges. They increase linearly towards the trench, where both the subducting and the overriding plates have an age of 40 Myr. The initial temperature profile follows the half-space cooling model (Supplementary Fig. S1). The surface and bottom thermal boundaries are isothermal at $T_s = 273$ K and $T_m = 1573$ K, respectively. The sidewalls are insulating (zero heat-flux). The top boundary is a free surface; all other boundaries are free-slip. A hanging slab tip (with a bending radius of 250 km, extending down to 194 km depth) is prescribed to initiate free subduction.

"Mantle" properties are ascribed to most of the simulation domain, except for a 7.5-km thick low-viscosity layer located along the top of the subducting plate, which allows for mechanical decoupling between the two plates. Both mantle and weak material have densities in a range relevant for mantle peridotite, with ρ_s of 3300 kg/m^3 at T_s. The density decreases with increasing temperature T, following

$$\rho = \rho_s \left[1 - \alpha (T - T_s) \right] \tag{4}$$

with α the coefficient of thermal expansion (3×10^{-5} K^{-1}).

The standard equations describing the conservation of mass, momentum and energy for an incompressible Stokes fluid under the Boussinesq approximation are solved within the Fluidity computational modeling framework (e.g. Davies et al., 2011; Kramer et al., 2012). This finite-element, control-volume code is built upon adaptive, unstructured discretizations (e.g. Davies et al., 2007), allowing to achieve a minimum element size of 400 m in regions of dynamical significance (in the present models, such mesh sizes are observed for instance in the decoupling layer), with coarser resolution elsewhere. The location of the decoupling layer, at the

interface between the subducting and overriding plates, is tracked using a volume fraction approach; its evolution is described by a linear advection equation. In order to avoid excessive numerical diffusion from the weak layer into neighboring regions, the former is discretized on the control volume mesh using the minimally diffusive HyperC face-value scheme (see Wilson (2009) for further details). We verified that the 7.5-km thick weak layer is well resolved, with near identical results obtained for simulations with a smaller minimum element size.

2.3. Composite viscosity and deformation partitioning

To solve the momentum equation, the rheological flow laws are implemented in Fluidity using a viscosity formulation. The effective viscosity μ_{eff} of the incompressible, isotropic material can be derived from rheological laws using (Gerya, 2010)

$$\mu_{eff} = \frac{\sigma_{II}}{2\dot{\varepsilon}_{II}} \tag{5}$$

with σ_{II} the second invariant (J_2) of the deviatoric stress tensor and $\dot{\varepsilon}_{II}$ the second invariant of the strain rate tensor defined in two-dimension as

$$\dot{\varepsilon}_{ij} = \frac{1}{2} \left(\frac{\partial v_i}{\partial x_j} + \frac{\partial v_j}{\partial x_i} \right) \tag{6}$$

The viscosity is modeled as controlled by three deformation mechanisms: diffusion creep, dislocation creep, and pseudo-brittle mechanism (noted with the subscript "*disl*", "*diff*" and "*br*" respectively in the following). The present approach considers that deformation is partitioned between the three coexisting deformation mechanisms (i.e. the individual strain rates add up; cf. chapter 3 in Frost and Ashby, 1982): $\dot{\varepsilon}_{tot} = \dot{\varepsilon}_{diff} + \dot{\varepsilon}_{disl} + \dot{\varepsilon}_{br}$. Accordingly, the corresponding bulk composite viscosity, μ, is calculated through a pseudo-harmonic mean:

$$\frac{1}{\mu} = \frac{1}{\mu_{diff}} + \frac{1}{\mu_{disl}} + \frac{1}{\mu_{br}} \tag{7}$$

with μ_{diff}, μ_{disl}, μ_{br} the viscosities associated with each deformation mechanism, as detailed below. Note that the composite viscosity corresponds to the lowest viscosity of the individual processes when differences between them are large. In the present models, the composite viscosity is bounded by upper and lower values of 10^{18} and 10^{25} Pa.s. There is no compositional difference between lithospheric and asthenospheric mantle material. The limits between slab/plate and surrounding asthenosphere arise and evolve naturally as a function of variations in the temperature and strain rate fields.

Following Moresi and Solomatov (1998), brittle failure at low pressure is approximated through the pseudo-brittle viscosity μ_{br}

$$\mu_{br} = \frac{\tau_y}{2\dot{\varepsilon}_{II}} \tag{8}$$

where τ_y is the yield strength derived from Byerlee's law:

$$\tau_y = \min(\tau_0 + f_c P, \tau_{y,\max}) \tag{9}$$

with τ_0 the cohesion at the surface (2 MPa), f_c the friction coefficient (0.2), P is the lithostatic pressure ($P = \rho_s g z$ where ρ_s is the reference density for mantle rocks, g the acceleration of gravity and z the depth), and $\tau_{y,\max}$ a maximum yield strength (10 GPa). The brittle strength of rock differs under extensive or compressive stresses, but in the present model, the pseudo-brittle viscosity μ_{br} only depends on the strain-rate second invariant $\dot{\varepsilon}_{II}$.

The viscosity in the diffusion creep regime is calculated as:

$$\mu_{diff} = A_{diff}^{-1} \exp\left(\frac{E_{diff} + P V_{diff}}{R(T + \delta T)}\right), \tag{10}$$

with R the gas constant. The activation energy E_{diff} and the activation volume V_{diff} are set to 410 kJ.mol^{-1} and 4 cm^3.mol^{-1}, respectively. The formulation of Eq. (10) accounts for a pressure-dependency, hence we also consider the depth-dependency of temperature by adding a δT to the Boussinesq temperature solution, calculated from an adiabatic gradient of 0.5 K/km. A_{diff} is 10^{-7} Pa.s, which corresponds to a constant grain size $d \sim 3$ mm, calculated with a pre-exponential factor of 1.5 10^{-15} Pa^{-1}.m^3 for diffusion creep in dry olivine in Hirth and Kohlstedt (2003). These values yield a viscosity for an asthenospheric layer deforming by diffusion creep between 10^{20} and 10^{21} Pa.s (see Supplementary Fig. S2). Note that the depth-dependency of the diffusion creep viscosity accounts for both increasing lithostatic pressure P and increasing temperature ($T + \delta T$) with increasing depth in the mantle. Supplementary Fig. S2 illustrates that the two effects counterbalance each other: diffusion creep viscosity calculated from Eq. (10) is almost depth-independent in the convective upper mantle.

The viscosity associated with deformation by diffusion (μ_{diff}) or dislocation creep (μ_{disl}) is calculated using Eq. (5). For dislocation creep, we implement Eq. (1) directly into Eq. (5) equating the differential stress and the uniaxial strain rate to the second invariants of deviatoric stress and strain rate tensors, respectively. This is a first-order approximation, which considers the rock as an isotropic material with a scalar (and not a tensor) viscosity. Moreover, deformation experiments (Eq. (1)) are often conducted under uniaxial loading (whereas stress is multidirectional in our 2-D models), and the differential stress (Eq. (1)) is different from the deviatoric stress (Eq. (5)) since the minimal applied stress is different from the mean stress (e.g. Schmalholz et al., 2019). The relationship between differential stress (Eq. (1)) and the second invariant of the deviatoric stress tensor (Eq. (5)) is given by Schmalholz et al. (2019) in 2-D: $\sigma_d = 2\sigma_{II}$; and by Gerya (2010) in 3-D: $\sigma_d = \sqrt{3}\sigma_{II} \approx 1.7\sigma_{II}$. The relationship between uniaxial strain rate to the second invariant of the strain rate tensor is $\dot{\varepsilon} = 2/\sqrt{3}\dot{\varepsilon}_{II} \approx 1.2\dot{\varepsilon}_{II}$ (Gerya (2010)). Implementing these corrections would lead to slightly smaller (by less a factor 2) mean viscosity for all three parameterizations, whereas the discrepancies between them are much larger (Fig. 4).

The weak layer deforms only by "yielding" with a reduced friction coefficient of 0.02 and its viscosity is capped at 10^{20} Pa.s. The weak layer properties revert to "mantle" properties below 200 km depth. The simulation is first run for a short time (<0.3 Myr) with only diffusion creep and "yielding" rheologies to generate non-zero strain rate and velocity fields that is identical for all simulations. The dislocation creep rheology (either *tanh*, *erf* or *algebraic* parameterization in Eq. (1)) is then introduced in the calculation of the bulk viscosity.

The partitioning of the deformation between the different mechanisms is calculated using the individual strain rates associated to each deformation mechanism:

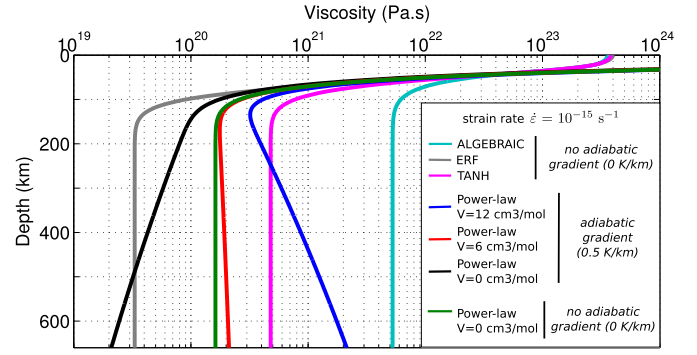$$\dot{\varepsilon}_y = \frac{\mu}{\mu_y}\dot{\varepsilon}_{tot}$$

Fig. 4. Vertical profiles of the dislocation creep viscosity under a 40-Myr old lithospheric plate (temperature profile shown in Supplementary Fig. S1), assuming a constant strain rate of 10^{-15} s^{-1}. The viscosity μ_{disl} is either calculated from combinations of Eq. (1), (2) and (5) (sigmoid functions *erf, tanh or algebraic*, see section 2.1) or from power-law expression in Eq. (13). The parameterization of the power-law cases is similar to the one used in Garel et al. (2014), with an activation energy E_{disl} of 540 kJ.mol^{-1}, an exponent n of 3.5, a pre-exponential factor A_{PL} of 4.4 10^{-17} Pa^{-n}s^{-1} and a additional temperature term δT calculated using an adiabatic gradient of 0.5 K/km. The activation volume is either 0 (black curve), 6 (red curve) or 12 cm^3.mol^{-1} (blue curve). Also shown is a case with no additional temperature term, i.e. adiabatic gradient of 0 K/km, and null activation volume (green curve).

$$\dot{\varepsilon}_{diff} = \frac{\mu}{\mu_{diff}}\dot{\varepsilon}_{tot} \tag{11}$$

$$\dot{\varepsilon}_{disl} = \frac{\mu}{\mu_{disl}}\dot{\varepsilon}_{tot}$$

We verify that the total strain rate equals the sum of all individual strain rates calculated in Eq. (11), consistently with the expression of the composite viscosity in Eq. (7). The individual strain rates are not used in the resolution of the conservation equations, which refers only to the bulk composite viscosity and the total strain rate. The expressions of Eq. (11) are solely used to discuss deformation partitioning. We consider that one mechanism dominates when its viscosity is much lower than the other two ($<20\%$), which corresponds to a strain rate much higher ($>80\%$) than these associated with the two other mechanisms. Equivalent deformation for all three mechanisms is not observed in our simulations. We quantify the deformation partitioning between the two coexisting creep mechanisms as the percentage of dislocation creep in total deformation p_{disl}:

$$p_{disl} = \frac{\dot{\varepsilon}_{disl}}{\dot{\varepsilon}_{diff} + \dot{\varepsilon}_{disl}} \tag{12}$$

3. Results

3.1. Subduction dynamics

Snapshots of the temperature, strain rate, and viscosity fields (top, middle and bottom panels, respectively) for each of the three dislocation creep parameterizations: *erf*, *tanh*, and *algebraic* (left, center and right columns) at the point when the 1300 K slab isotherm reaches 400 km depth are presented in Fig. 5. This point in the simulation is characterized by a rapid sinking of the slab in the upper mantle, before the descent is hampered by the bottom boundary at 660 km. The three parameterizations lead to distinct subduction dynamics, with the slab reaching 400 km depth in 0.7, 5.0, and 11.9 Myr, for the *erf*, *tanh*, and *algebraic* parameterizations, respectively. A quantitative comparison of key subduction diagnostic features is provided is Table 1. Although the average temperature in the asthenosphere is the same in all three cases,
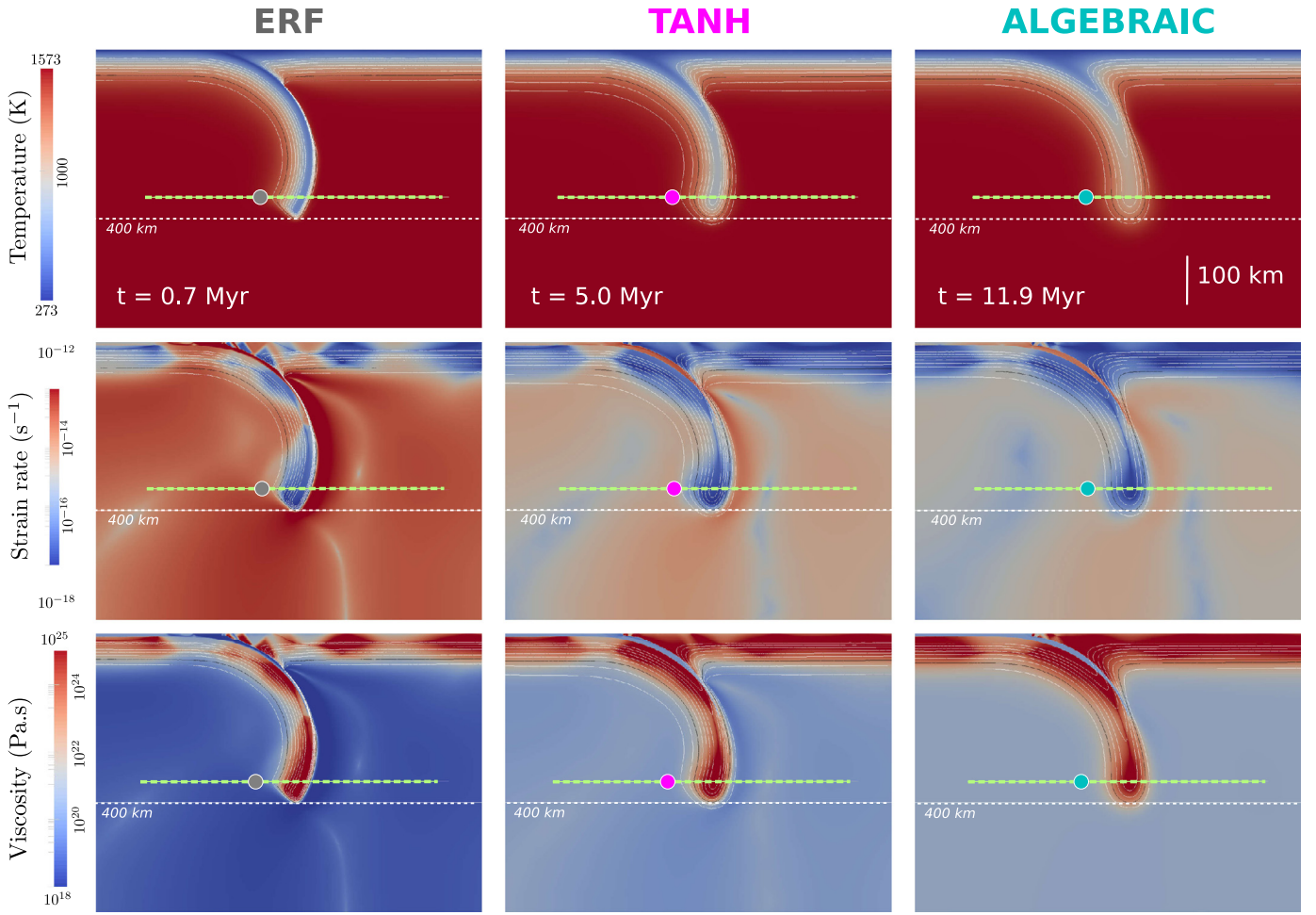
Fig. 5. Snapshots of the temperature (top) strain rate (middle) and viscosity (bottom) fields in a domain surrounding the subducting slab when the 1300 K isotherm reaches 400 km depth for simulations using the three different dislocation creep parameterizations: *erf* (left), *tanh* (center) and *algebraic* (right). The dashed green lines show the cross section along which profiles are extracted in Fig. 6. The isotherms are drawn 100 K apart (white lines), the black line is the 1300 K isotherm.

Table 1
Quantitative comparisons between the simulations with either of the three dislocation creep parameterizations (*erf*, *tanh*, and *algebraic*) when the slab (isotherm 1300 K) reaches 400 km depth, corresponding to Figs. 5, 6 and 7. The diffusive length is calculated with a thermal diffusivity of 10^{-6} m^2.s^{-1}.

	ERF	TANH	ALGEBRAIC
Time (Myr)	0.7	5.0	11.9
Associated diffusive length (km)	5	13	19
Width of slab at 350 km (distance between 1500-K isotherms)	113	126	141
Minimum slab temperature at 350 km depth (K)	586	854	1034
Subducting plate velocity (cm/yr)	223	5.1	1.5
Mean asthenosphere viscosity (Pa.s) below 200 km depth (averaged for temperatures >1500 K)	8.0 10^{18}	2.2 10^{20}	3.8 10^{20}
Slab mean viscosity below 200 km depth (T < 1300 K)	4.5 10^{24}	3.2 10^{24}	2.4 10^{24}

the thermal structure of the cold slab varies: slab width and thermal structure are influenced by thermal diffusion, the magnitude of which depends on the elapsed time and, hence, on the slab sinking velocity. As a consequence, by the time the fast-sinking *erf* slab reaches 400 km depth, its thermal structure has only been slightly modified, whereas the temperature contrast between slab and asthenosphere has been smoothed in both *tanh* and *algebraic* parameterizations. The strain rate field also reflects the distinct subduction dynamics: in the *erf* simulation, large strain rates in the asthenosphere far away from the slab (about 10^{-13} s^{-1}) arise in response to the strong viscous drag induced by the rapidly sinking slab. Strain rates in the asthenosphere are ∼100 times smaller in the *tanh* and *algebraic* simulations, the latter exhibiting

the smallest strain rates. Asthenosphere viscosities (bottom panel of Fig. 5) are in the same order of magnitude for *tanh* and *algebraic* cases (∼10^{20} Pa.s), but significantly lower for the *erf* case (<10^{19} Pa.s).

Horizontal profiles of temperature, strain rate, and viscosity at 350 km depth for the three simulations at the times shown on Fig. 5 are presented in Fig. 6. The profiles are located so that the cross-section is far away from both the slab tip and the base of the surface lithospheric plate. The slab is visible on the thermal profiles as colder temperatures in comparison to the surrounding asthenosphere, which has an average temperature of 1573 K. The asymmetrical temperature profile in the *erf* case is inherited from the initial surface plate thermal structure, as opposed to the sym-
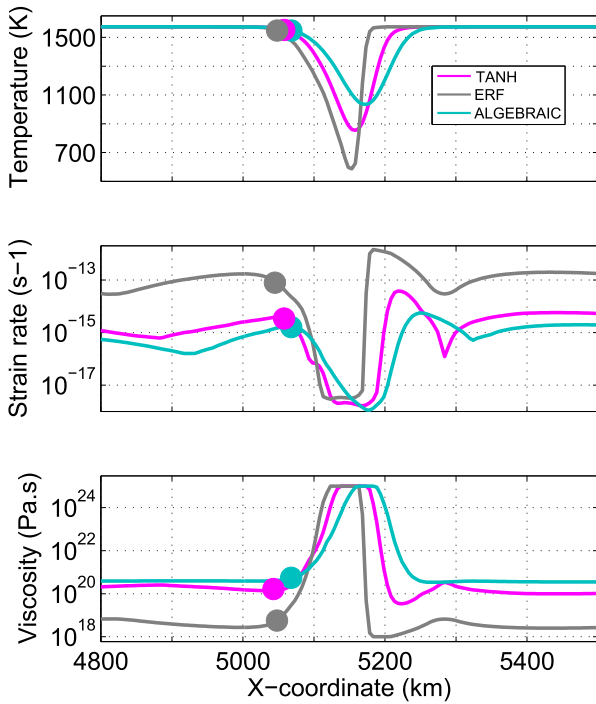
Fig. 6. Temperature (top), strain rate (middle) and viscosity (bottom) horizontal profiles across the slab at 350 km depth when the slab isotherm 1300 K reaches 400 km depth. The profiles are drawn between $X = 4800$ km and $X = 5500$ km (dashed lines in Fig. 5) for the three simulations (*erf*, *tanh* and *algebraic*), with filled circle markers located in the asthenosphere close to the slab as shown in Fig. 5.

metrical thermal profiles in the *tanh* and *algebraic* cases, which have been smoothed by thermal diffusion (Fig. 6, top panel). The coldest temperature in the slab is related to the time elapsed since subduction started. It is 584 K for the *erf* slab that has subducted to 400 km depth in 0.7 Myr old, 854 K for the *tanh* slab that has subducted to 400 km depth in 5 Myr, and 1034 K for the *algebraic* slab that has subducted to 400 km depth in 12 Myr. The cold slab core is the least deformed region (Fig. 6, middle panel). The contrast in strain rate and viscosity between the slab and the surrounding asthenosphere depends strongly on the parameterization and is not solely a function of spatial variations in temperature (cf. top and middle/bottom panels in Fig. 6). As already highlighted in Fig. 5, asthenospheric strain rates in the erf case (up to 10^{-12} s^{-1}) are up to three orders of magnitude higher than in the *tanh* and *algebraic* cases (10^{-16}–10^{-15} s^{-1}). The *erf* simulation presents a thick undeformed cold slab core (characterized by strain rates of 10^{-18} s^{-1}), and a fast deforming asthenosphere (strain rates of 10^{-13} s^{-1}). A region in the mantle wedge strongly deformed by viscous drag is visible on the right side of the slab in Figs. 5 and 6 for all simulations. Strain rates in this layer are the highest in the *erf* simulation and the lowest in the *algebraic* case, the latter exhibiting the weakest contrasts in strain rate and viscosity between slab and asthenosphere. The viscosity profiles further illustrate the combined influence of the strain rate and temperature. The discrepancy between asthenospheric viscosities ($\sim 10^{18-19}$ Pa.s in the *erf* case and $\sim 10^{20-21}$ Pa.s in the other cases) reflects the variation in strain rates between the three simulations.

3.2. Partitioning of deformation between dislocation and diffusion creep

The partitioning of deformation between the different mechanisms considered here (diffusion or dislocation creep, or pseudo-brittle yielding – see partitioning definition in section 2.3) is presented in Fig. 7, in a similar way as in Cizkova et al. (2007), Garel et al. (2014) and Bessat et al. (2020), even if the latter

only highlight the mechanism yielding the minimum viscosity rather than their relative importance. Pseudo-brittle yielding only dominates near the surface and at the subduction interface. For the *erf* parameterization, deformation occurs almost everywhere by dislocation creep only, except for the cold core of the slab, which is at the maximum cut-off viscosity. In contrast, for the *algebraic* case, deformation in most of the asthenosphere mantle occurs dominantly through diffusion creep; dislocation creep only predominates within and around the cold slab. In the *tanh* case, both dislocation and diffusion creep contribute to deformation in most of the asthenosphere and dislocation creep prevails within and around the slab, as well as in most of the lithosphere-asthenosphere boundary. Comparing Figs. 5 and 7 allows us to relate the differences in asthenospheric viscosity between the three parameterizations to changes in the dominantly activated deformation mechanism: the low viscosity in *erf* simulation results from the strain rate dependence of dislocation creep, which leads to weakening in presence of high strain rates, whereas the high viscosity in the *algebraic* simulation reflects the lack of strain rate dependence in a medium deforming dominantly by diffusion creep. However, the same asthenospheric viscosity can arise from different combinations of rheological parameterizations: similar viscosities ($\sim 10^{20}$ Pa.s) are produced by activation of both creep processes in *tanh* simulation and by dominant diffusion creep in the *algebraic* case.

The strain rate and temperature conditions at which strain rate is equally partitioned between dislocation and diffusion creep at 350 km depth for each of the three parameterizations are depicted in Fig. 8. Note that this partitioning depends on the chosen diffusion creep parameters (e.g. grain size). The evolution of strain rate as a function of temperature (Fig. 8) highlights the sensitivity of deformation partitioning to both diffusion and dislocation creep parameterizations in the convecting asthenosphere, whereas Fig. 2 showed only the dislocation creep sensitivity. For the rheological parameterizations used in this study, diffusion creep prevails at low strain rates, and dislocation creep prevails at high strain rates. At low temperature, the three dislocation parameterizations predict similar behaviors. However, the predictions diverge for temperatures higher than 1100 K (i.e. at conditions prevailing in the asthenosphere and at the base of the lithospheric plates). For example, at 1550 K and 350 km depth, the strain rate required for an equal partitioning between diffusion creep and dislocation creep is $2*10^{-18}$ s^{-1} for the *erf* case, $9*10^{-16}$ s^{-1} for the *tanh* case, and 10^{-14} s^{-1} for the *algebraic* case. Thus, dependency of the effective viscosity on strain rate, through the activation of dislocation creep, appears at much lower strain rates in the *erf* case than in the *algebraic* case. This difference results solely from the mathematical parameterizations (Eq. (1)).

The initial asthenosphere strain rate and temperature conditions (3×10^{-16} s^{-1}, 1573 K) for a point at 350 km depth at the time when dislocation creep is "switched on" in the simulations (cf. section 2.2) is indicated as a black square in Fig. 8. For these strain rate and temperature conditions, the amount of deformation accommodated by dislocation creep is $p_{disl} = 87$, 24, or 2% for the *erf*, *tanh*, or *algebraic* parameterizations. The partitioning evolves through time, with colored dots in Figs. 5, 6, and 8 locating the conditions at the time when the slab reaches 400 km depth. The differences in deformation partitioning have been enhanced: the contribution of dislocation creep in the near-slab asthenosphere is larger in all simulations. The contribution of dislocation creep is larger, both in terms of magnitude and of volume of material, in the *erf* case ($p_{disl} = 99\%$) than in the *tanh* ($p_{disl} = 73\%$) and *algebraic* ($p_{disl} = 15\%$) cases, explaining the contrasted deformation maps in Fig. 7. The differences between the three parameterizations, already visible in Fig. 2, are obvious from Fig. 8: either for the initial or later times in the simulations, the deformation occurs
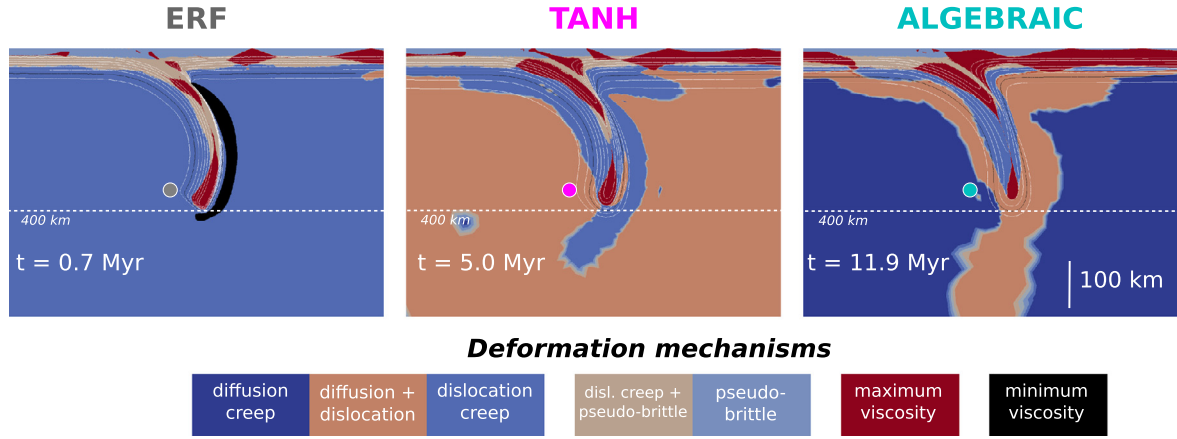

Deformation mechanisms

| diffusion creep | diffusion + dislocation | dislocation creep | disl. creep + pseudo-brittle | pseudo-brittle | maximum viscosity | minimum viscosity |

Fig. 7. Maps of deformation mechanisms as a function of local strain rate and temperature conditions, representing the deformation partitioning between the different deformation mechanisms. Mechanisms are indicated depending on their respective contributions to total deformation (see section 2.3 for details). The spatial domain is the same as in Fig. 5, for the three simulations: *erf* (left), *tanh* (center) and *algebraic* (right). The minimum (resp. maximum) viscosity of 10^{18} (resp. 10^{25}) Pa.s, occurs in the highly deformed asthenosphere around the slab in the *erf* case (resp. in coldest and least deformed lithosphere domains).
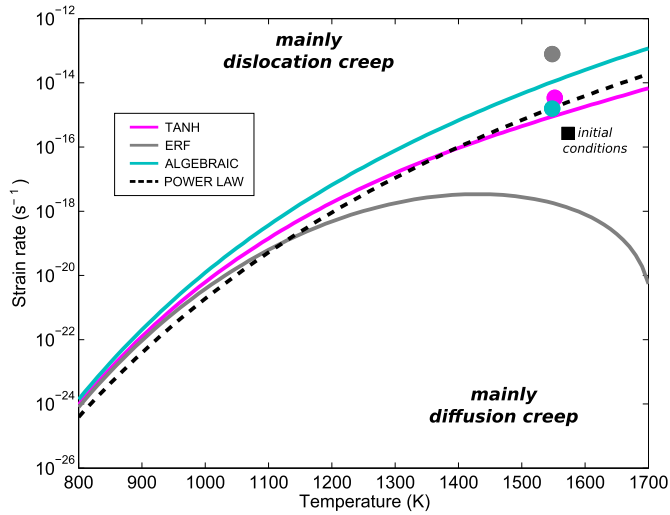

Fig. 8. Strain rate and temperature conditions at which the deformation at 350 km depth is equally partitioned between diffusion creep and dislocation creep. The lines are drawn for the three dislocation creep parameterizations (*erf*, *tanh* and *algebraic*), and for a power-law expression of dislocation creep (Eq. (3) with parameters from Gouriet et al., 2019). Dislocation creep prevails at high strain rates, whereas diffusion creep prevails at low strain rates. The filled circle symbols are located in the near-slab asthenosphere as shown in Figs. 5 and 7. The black square represents the initial conditions at that location, identical for all three simulations ($3\ 10^{-16}$ s^{-1}, 1573 K).

mainly by diffusion creep in the *algebraic* case, mainly in dislocation creep in the *erf* case, and by a balanced mixture of the two in the *tanh* case, as illustrated in Supplementary Material Fig. S3.

The deformation partitioning as a function of temperature and strain rate for a power law parameterization of dislocation creep (Eq. (3)) is also shown in Fig. 8. The *tanh* parameterization is closer to the power law than to the two others. However, stresses higher than 150 MPa are predicted in the cold slab and surface plates (Supplementary Fig. S4 and Cizkova et al., 2007). In these regions, the power-law is not suitable to describe dislocation creep (cf. Fig. 2 of Gouriet et al. (2019)). Another illustration of the limitation of the classical powerlaw formulation of Eq. (3) is shown in Supplementary Fig. S6 depicting the variation of the apparent stress exponent *n* as a function of temperature and strain rate for the three parameterizations: *n* increases with decreasing temperature, with values higher than 10 at low-temperature values, as predicted for an exponential flow law by Schmalholz and Fletcher

(2011), and *n* tends to a value of 1 (i.e. diffusion creep) at high temperature and low strain rates.

4. Discussion

4.1. Comparison to large-scale constraints on mantle and plate dynamics

The predictions of the present simulations can be compared to a number of different observations. First, surface plate velocities reconstructed from paleomagnetic data and recorded through GPS are generally less than 10–15 cm/yr and have not often exceeded this over the past 200 Ma (e.g. Müller et al., 2008; Larson et al., 1997). This rules out extremely fast-sinking slabs (>200 cm/yr), such as those obtained in the *erf* case. Second, some slabs seem to penetrate deep into the mantle (>1000 km) as imaged by seismic tomography (e.g. Li et al., 2008). This implies that slabs temperature remains sufficiently low to induce faster than average seismic velocities. Such an observation is consistent with the slab temperatures in the *erf* and *tanh* cases, but not with the slow and wide slab in the *algebraic* simulation, which already exhibits a core hotter than 900 K at 150-km depth (Fig. 5).

Estimates of the mean upper mantle viscosity have been derived from a number of independent observations, including glacial isostatic adjustment (e.g. Paulson and Richards, 2009), long-wavelength geoid observations combined with surface plate velocities (e.g. Ricard and Vigny, 1989), constraints from Pacific plate dynamics (e.g. Iaffaldano and Lambeck, 2014; Stotz et al., 2018), or melting conditions above mantle plumes (e.g. Thoraval et al., 2006). These different approaches yield viscosities between $\sim10^{20}$ and $\sim10^{21}$ Pa.s, which are incompatible with the very weak asthenosphere in the *erf* case, but consistent with the results using either *tanh* or *algebraic* parameterizations (Fig. 4). Moreover, the *tanh* simulations show that mantle viscosity can locally be as low as 10^{19} Pa.s in highly deforming regions (e.g. plate base and slab vicinity in Fig. 5). These values meet the viscosity needed to activate processes such as the small-scale convection that is necessary to explain: (i) the surface heat flow in old oceanic plates (e.g. Dumoulin et al., 2005); (ii) high surface heat-flow and thin lithosphere observed in many back-arc regions (e.g. Currie and Hyndman, 2006; Davies et al., 2016) or to account for post-seismic surface deformation (Klein et al., 2016).

Global seismic anisotropy measurements using surface waves point to strong radial and azimuthal anisotropy in the lithosphere and asthenosphere and to a decrease in the intensity of the

anisotropy at depths higher than 250 km (Montagner and Kennett, 1996). This observation may be explained by a change in the dominant dislocation slip systems of olivine, from dominant [100] dislocation to dominant glide of [001] dislocation with increasing pressure in an upper mantle deforming dominantly by dislocation creep (Mainprice et al., 2005). However, it is also consistent with a decrease in the contribution of dislocation creep with increasing depth in a convective mantle deforming by a mixture of dislocation and grain-size sensitive processes, represented here by the implementation of diffusion creep, as in the *tanh* simulations (Fig. 7), if one considers that such processes do not produce olivine crystal preferred orientations. Yet this assumption has been recently challenged by numerical models (Wheeler, 2009) and creep experiments (Miyazaki et al., 2013) in which olivine crystal and shape preferred orientations developed during deformation by diffusion creep at high temperature (>1473 K).

Gouriet et al. (2019) modeled the rheology of a single crystal of olivine well-oriented for dislocation glide. Olivine is only stable up to 410 km. Hence, using the parameterization of Eq. (1) for both the upper mantle and the transition zone in our simulations is an approximation. We try to limit its effect by analyzing the results only up to the time at which the slab penetrates into the transition zone. The dynamics of the simulations will likely be modified by considering a more realistic, higher strength rheology in the transition zone (Ritterbex et al., 2016), but the contrasts between the simulations with different parameterizations will remain.

4.2. Physical feedbacks in subduction dynamics

Our results demonstrate that distinct subduction regimes (Fig. 5) can arise from small discrepancies between rheological parameterizations (Fig. 2). The geodynamical simulations thus appear to be an appropriate tool for unraveling the first-order physical processes at stake. Two feedback loops coupled through slab dynamics are described in Fig. 9. The slab sinking velocity is controlled both by the buoyancy of the slab itself and by the viscosity of the surrounding asthenosphere (viscous resistance). A first feedback is related to the heating and widening of the slab through thermal diffusion, which is a time-dependent process. The resistance of asthenosphere to slab penetration increases with slab surface area, which is itself controlled by the time-integrated thermal diffusion. Furthermore, temperature controls the slab density contrast and buoyancy relative to the surrounding asthenosphere. Hence, the slower the slab, the larger the diffusion length, the wider and the hotter the slab, and the slower the sinking (e.g. *algebraic* case in Fig. 5).

A second feedback arises when the mantle viscosity is strain rate dependent, i.e. when a large part of the total deformation is accommodated through dislocation creep (*erf* and *tanh* cases in Fig. 7). In this case, viscous drag driven by the sinking slab induces large strain rates in the asthenosphere, which weakens via dislocation creep and, in turn, accelerates slab sinking. This rheological feedback is only weakly active in the *algebraic* simulation: in the absence of asthenosphere weakening, slow subduction dynamics is mainly controlled by the thermal feedback loop (Fig. 9). In contrast, asthenospheric weakening due to dislocation creep is very efficient in the *erf* case: thermal diffusion is too slow relatively to fast slab sinking velocities. For the *tanh* parameterization, the rheological feedback is substantial, but does not overwhelm the thermal feedback, because the range of asthenospheric strain rates (10^{-17}–10^{-13} s^{-1}, Fig. 5) corresponds to intermediate p_{disl} values (30–70%).

It is interesting to calculate a mean time for a slab to reach the transition zone, which is more than 3 Myr at the velocities inferred from observations (<15 cm/yr). This minimum time corresponds
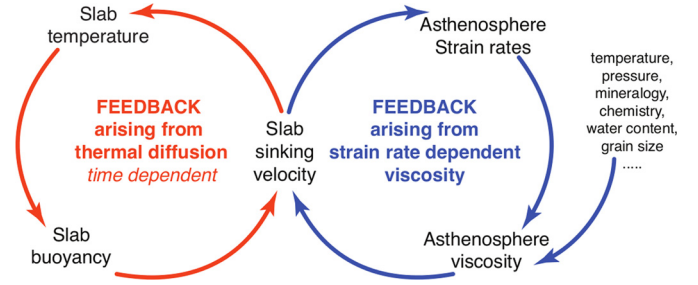

Fig. 9. Feedback loops between slab sinking dynamics and either (i) slab thermal structure (left) or (ii) asthenosphere viscosity (right). Their interactions depend on the interplay between the strain rate dependent and strain rate independent viscosities, e.g. dislocation creep and diffusion creep, respectively, in the simulations (see section 4.3 for details).

to a minimum diffusive length of 10 km using a thermal diffusivity of 10^{-6} m^2/s as in our simulations.

This suggests that the viscosity in the asthenosphere is ultimately constrained from slab sinking velocities, which should lead to balanced thermal and dynamical feedbacks loops (Fig. 9). This rules out results obtained in this study for *erf* (i.e. too rapid sinking) and *algebraic* parameterizations (i.e. too slow).

4.3. Constraining effective mantle viscosity using geodynamical simulations

The *tanh* parameterization provides both a satisfactory description of the dislocation creep process in olivine observed in the dislocation dynamics simulations of Gouriet et al. (2019) (Fig. 2) and large-scale subduction dynamics predictions that fulfill many important observational constraints (section 4.1). The effective asthenosphere viscosity, which is key for plate dynamics as explained in Fig. 9, results from coexisting deformation mechanisms. In our study, the mild, steady partitioning of dislocation vs. diffusion creep in the *tanh* case ensures that the feedback based on strain rate dependent viscosity is activated and does not bolt out.

However, we acknowledge that subduction dynamics compatible with large-scale observables could also arise with different rheological parameterizations. For instance, diffusion creep, which seems to control the asthenosphere viscosity and slab sinking rate (Fig. 9), depends on an assumed grain size (e.g. Hirth and Kohlstedt, 2003).

Furthermore, our parameterization of dislocation creep (Eq. (1)) does not feature any depth-dependency, whereas laboratory deformation experiments suggest a dependence on confining pressure (Hirth and Kohlstedt, 2003). This feature is accounted for through the term "PV_{disl}" in the general power-law expression, similar to Eq. (3):

$$\dot{\varepsilon} = A_{PL}\sigma_d^n \exp\left(-\frac{E_{disl} + PV_{disl}}{R(T + \delta T)}\right) \tag{13}$$

with the depth-dependency of temperature included in the term δT as in Eq. (10). Vertical profiles of the dislocation creep viscosity calculated from Eq. (13) are compared to the sigmoid ones calculated from Eq. (1) and Eq. (5) in Fig. 4, for various values of activation volumes and adiabatic gradients. The higher the activation volume, the larger the rate of viscosity increase with depth, whereas the adiabatic increase of temperature decreases the viscosity with depth. As for diffusion creep (Supplementary Fig. S2), the combination of non-zero activation volume and thermal gradient can lead to a quasi-constant viscosity in the mantle below the plates (red curve on Fig. 4). In this study, the pressure-independent rheology derived from Eq. (1) corresponds thus to the first-order assumption that the mean asthenosphere viscosity does not vary

with depth for constant strain-rate conditions. This assumption may also be justified by the present uncertainty on the vertical variations of viscosity in the upper mantle, for which geophysical and geological constraints yield non-unique solutions (as shown in Cizkova et al., 2012 – their Fig. 1).

There are many sources of uncertainty in the determination of flow laws. The first one arises from the adjustment of the semi-empirical equations to fit the experimental mechanical data (e.g. Ashby and Verrall, 1978; Bai et al., 1991; Hirth and Kohlstedt, 2003). This affects in particular the pre-exponential factor A in both diffusion and dislocation creep flow laws, but also the other constants (e.g. activation energy and activation volume) in Eq. (10) and (13). There is also a large dispersion in the experimental data itself, due to differences in initial material (hot press of fine-powder olivine or sol-gel pure forsterite) and experimental conditions (torsion, axial compression, temperature range), which could lead to different associations of deformation processes (cf. the difference in dislocation creep strength between natural dunites and synthetic olivine polycrystals produced by different methods – see references in Demouchy et al., 2013).

Large uncertainties also arise from the extrapolation of the experimentally derived parameterizations over orders of magnitude in strain rate and grain sizes (from microns to millimeters) and from the lack of external constraints on the actual values of important parameters, such as the grain sizes in the asthenospheric mantle. For dislocation creep, the former limitation has been partially overcome by the use of numerical models, such as Boioli et al. (2015) and Gouriet et al. (2019) to avoid the extrapolation to geological strain rates. However, these models are still limited to single crystals. The behavior of a rock, that is a polycrystal, differs: the rock will be stronger by a factor 2-50, which depends on the orientation of olivine crystals, evolving with strain (e.g. Tommasi et al., 2000; Mameri et al., 2019). Other processes than pure dislocation or diffusion creep, such as coupled grain boundary migration and shear (Mompiou et al., 2009; Cordier et al., 2014) or grain-boundary sliding (e.g., Maruyama and Hiraga, 2017) may also play a role during the deformation of a polycrystalline aggregate at depth.

In brief, the enormous experimental investment in the determination of flow laws for the upper mantle produced strong constraints on the deformation processes, on the equations describing the associated mechanical behavior, and on the range of physical parameters controlling their activation. However, we are still far from having robust and unique predictions of its rheology (or of any other layer in the Earth). The present study shows that geodynamical models may be used as a complementary tool for handling the question. They cannot discriminate the best one among different parameterizations, but they can determine which combinations of flow laws and their parameters produce Earth-like large-scale dynamics, thus constraining the effective mantle viscosity.

5. Conclusions

The results of numerical experiments of dislocation dynamics in olivine have been used to derive three different sigmoid parameterizations (*erf, tanh, algebraic*) describing the variation of stress as a function of strain rate and temperature, relevant for a wide range of stress and temperature conditions prevailing in both asthenospheric and lithospheric mantle. These dislocation creep parameterizations were then implemented, together with a classical diffusion creep law, in numerical models of subduction dynamics.

While the three parameterizations fit well the dislocation dynamics results (Fig. 2), the *tanh* parameterization yields subduction dynamics that is most compatible with the large-scale observables (e.g. surface plate velocities, mantle viscosity, seismic imaging). In this case, the feedback between slab dynamics and asthenospheric viscosity, which is strain rate dependent due to activation of dislocation creep, is modulated by the effect of thermal diffusion. There is a strong weakening due to dislocation creep in region of high stresses or high strain rates. However, most of the convective mantle in the *tanh* case deforms by a mixture of strain rate dependent (here dislocation creep) and strain rate independent (here diffusion creep) processes that maintains a balance between dynamical and thermal feedbacks (Fig. 9). The other two parameterizations, *erf* and *algebraic*, can here be ruled out from the comparison with large-scale constraints on mantle and plate dynamics, since they are associated with too fast or too slow slab sinking due to a too large or too small contribution of dislocation creep to the total deformation, respectively.

Subduction dynamics depends on asthenosphere viscosity. The effective viscosity in the present thermo-mechanical models results from interplay between different deformation mechanisms. The sensitivity to rheological parameterizations is tremendous, yielding distinct dynamics even for deviations within the range of uncertainty of the experimental data. However, large-scale observables provide important constraints on plate and mantle dynamics, which makes the derivation of an effective mantle viscosity robust. This viscosity can be reproduced by a variety of combinations of parameterizations of deformation processes. For instance, a unified rheology expression including a variable stress exponent n, as proposed by Cordier et al. (2012) for lower mantle MgO and analogue to the apparent n exponent in Fig. S6, is a possible lead to account for strain rate dependent and independent viscosities at once. We hence recommend testing rheological laws in geodynamical thermo-mechanical models to evaluate the interplay and possible feedbacks between different deformation processes and thermal diffusion; such tests ensuring the large-scale dynamical consistency of the chosen rheological laws.

Declaration of competing interest

The authors declare that they have no known competing financial interests or personal relationships that could have appeared to influence the work reported in this paper.

Appendix A. Supplementary material

Supplementary material related to this article can be found online at https://doi.org/10.1016/j.epsl.2020.116243.

References

Ashby, M.F., Verrall, R., 1978. Micromechanisms of flow and fracture, and their relevance to the rheology of the upper mantle. Philos. Trans. R. Soc. Lond. Ser. A, Math. Phys. Sci. 288, 59–95. https://doi.org/10.1098/rsta.1978.0006.

Bai, Q., Mackwell, S., Kohlstedt, D., 1991. High-temperature creep of olivine single crystals 1. Mechanical results for buffered samples. J. Geophys. Res., Solid Earth 96, 2441–2463. https://doi.org/10.1029/90JB01723.

Baumann, T., Kaus, B.J., 2015. Geodynamic inversion to constrain the non-linear rheology of the lithosphere. Geophys. J. Int. 202, 1289–1316. https://doi.org/10.1093/gji/ggv201.

Bessat, A., Duretz, T., Hetenyi, G., Pilet, S., Schmalholz, S.M., 2020. Stress and deformation mechanisms at a subduction zone: insights from 2-D thermo-mechanical numerical modelling. Geophys. J. Int. 221, 1605–1625. https://doi.org/10.1093/gji/ggaa092.

Boioli, F., Tommasi, A., Cordier, P., Demouchy, S., Mussi, A., 2015. Low steady-state stresses in the cold lithospheric mantle inferred from dislocation dynamics models of dislocation creep in olivine. Earth Planet. Sci. Lett. 432, 232–242. https://doi.org/10.1016/j.epsl.2015.10.012.

Cizkova, H., van Hunen, J., van den Berg, A., 2007. Stress distribution within subducting slabs and their deformation in the transition zone. Phys. Earth Planet. Inter. 161, 202–214. https://doi.org/10.1016/j.pepi.2007.02.002.

Cizkova, H., van den Berg, A.P., Spakman, W., Matyska, C., 2012. The viscosity of Earth's lower mantle inferred from sinking speed of subducted lithosphere. Phys. Earth Planet. Inter. 200, 56–62. https://doi.org/10.1016/j.pepi.2012.02.010.

Cordier, P., Amodeo, J., Carrez, P., 2012. Modelling the rheology of MGO under Earth's mantle pressure, temperature and strain rates. Nature 481, 177–180. https://doi.org/10.1038/nature10687.

Cordier, P., Demouchy, S., Beausir, B., Taupin, V., Barou, F., Fressengeas, C., 2014. Disclinations provide the missing mechanism for deforming olivine-rich rocks in the mantle. Nature 507, 51–56. https://doi.org/10.1038/nature13043.

Crameri, F., Kaus, B.J., 2010. Parameters that control lithospheric-scale thermal localization on terrestrial planets. Geophys. Res. Lett. 37. https://doi.org/10.1029/2010GL042921.

Currie, C.A., Hyndman, R.D., 2006. The thermal structure of subduction zone back arcs. J. Geophys. Res., Solid Earth 111. https://doi.org/10.1029/2005JB004024.

Davies, D.R., Davies, J.H., Hassan, O., Morgan, K., Nithiarasu, P., 2007. Investigations into the applicability of adaptive finite element methods to two-dimensional infinite Prandtl number thermal and thermochemical convection. Geochem. Geophys. Geosyst. 8, Q05010. https://doi.org/10.1002/2015GC006125.

Davies, D., Le Voci, G., Goes, S., Kramer, S.C., Wilson, C.R., 2016. The mantle wedge's transient 3-D flow regime and thermal structure. Geochem. Geophys. Geosyst. 17, 78–100. https://doi.org/10.1029/2006GC001470.

Davies, D.R., Wilson, C.R., Kramer, S.C., 2011. Fluidity: a fully unstructured anisotropic adaptive mesh computational modeling framework for geodynamics. Geochem. Geophys. Geosyst. 12, Q06001. https://doi.org/10.1029/2011GC003551.

Demouchy, S., Tommasi, A., Ballaran, T.B., Cordier, P., 2013. Low strength of Earth's uppermost mantle inferred from tri-axial deformation experiments on dry olivine crystals. Phys. Earth Planet. Inter. 220, 37–49. https://doi.org/10.1016/j.pepi.2013.04.008.

Dumoulin, C., Doin, M.P., Arcay, D., Fleitout, L., 2005. Onset of small-scale instabilities at the base of the lithosphere: scaling laws and role of pre-existing lithospheric structures. Geophys. J. Int. 160, 344–356. https://doi.org/10.1111/j.1365-246X.2004.02475.x.

Evans, B., Goetze, C., 1979. The temperature variation of hardness of olivine and its implication for polycrystalline yield stress. J. Geophys. Res., Solid Earth 84, 5505–5524. https://doi.org/10.1029/JB084iB10p05505.

Frost, H.J., Ashby, M.F., 1982. Deformation Mechanism Maps: The Plasticity and Creep of Metals and Ceramics. Pergamon Press.

Garel, F., Goes, S., Davies, D., Davies, J.H., Kramer, S.C., Wilson, C.R., 2014. Interaction of subducted slabs with the mantle transition-zone: a regime diagram from 2-D thermo-mechanical models with a mobile trench and an overriding plate. Geochem. Geophys. Geosyst. 15, 1739–1765. https://doi.org/10.1002/2014GC005257.

Gerya, T., 2010. Introduction to Numerical Geodynamic Modelling. Cambridge University Press. 345 pp https://doi.org/10.1017/CBO9780511809101.

Gouriet, K., Cordier, P., Garel, F., Thoraval, C., Demouchy, S., Tommasi, A., Carrez, P., 2019. Dislocation dynamics modelling of the power-law breakdown in olivine single crystals: toward a unified creep law for the upper mantle. Earth Planet. Sci. Lett. 506, 282–291. https://doi.org/10.1016/j.epsl.2018.10.049.

Hirth, G., Kohlstedt, D., 2003. Rheology of the upper mantle and the mantle wedge: a view from experimentalists. In: Inside the Subduction Factory. In: Geophys. Monogr., vol. 138, pp. 83–105. https://doi.org/10.1029/138GM06.

van Hunen, J., van den Berg, A.P., Vlaar, N.J., 2000. A thermo-mechanical model of horizontal subduction below an overriding plate. Earth Planet. Sci. Lett. 182, 157–169. https://doi.org/10.1016/S0012-821X(00)00240-5.

Iaffaldano, G., Lambeck, K., 2014. Pacific plate-motion change at the time of the Hawaiian-Emperor bend constrains the viscosity of Earth's asthenosphere. Geophys. Res. Lett. 41, 3398–3406. https://doi.org/10.1002/2014GL059763.

Kárason, H., Van Der Hilst, R.D., 2000. Constraints on mantle convection from seismic tomography. In: The History and Dynamics of Global Plate Motion. In: Geophys. Monogr., vol. 121, pp. 277–288. https://doi.org/10.1029/GM121p0277.

Klein, E., Fleitout, L., Vigny, C., Garaud, J., 2016. Afterslip and viscoelastic relaxation model inferred from the large-scale post-seismic deformation following the 2010 Mw 8.8 Maule earthquake (Chile). Geophys. J. Int. 205, 1455–1472. https://doi.org/10.1093/gji/ggw086.

Kramer, S.C., Wilson, C.R., Davies, D.R., 2012. An implicit free surface algorithm for geodynamical simulations. Phys. Earth Planet. Inter. 194, 25–37. https://doi.org/10.1016/j.pepi.2012.01.001.

Larson, K.M., Freymueller, J.T., Philipsen, S., 1997. Global plate velocities from the global positioning system. J. Geophys. Res., Solid Earth 102, 9961–9981. https://doi.org/10.1029/97JB00514.

Li, C., van der Hilst, R.D., Engdahl, E.R., Burdick, S., 2008. A new global model for P wave speed variations in Earth's mantle. Geochem. Geophys. Geosyst. 9, Q05018. https://doi.org/10.1029/2007GC001806.

Mainprice, D., Tommasi, A., Couvy, H., Cordier, P., Frost, D.J., 2005. Pressure sensitivity of olivine slip systems and seismic anisotropy of Earth's upper mantle. Nature 433, 731–733. https://doi.org/10.1038/nature03266.

Mameri, L., Tommasi, A., Signorelli, J., Hansen, L.N., 2019. Predicting viscoplastic anisotropy in the upper mantle: a comparison between experiments and polycrystal plasticity models. Phys. Earth Planet. Inter. 286, 69–80. https://doi.org/10.1016/j.pepi.2018.11.002.

Maruyama, G., Hiraga, T., 2017. Grain-to multiple-grain-scale deformation processes during diffusion creep of forsterite + diopside aggregate: 1. Direct observations. J. Geophys. Res., Solid Earth 122, 5890–5915. https://doi.org/10.1002/2017JB014254.

McKenzie, D., Jackson, J., Priestley, K., 2005. Thermal structure of oceanic and continental lithosphere. Earth Planet. Sci. Lett. 233, 337–349. https://doi.org/10.1016/j.epsl.2005.02.005.

Melosh, H., Fleitout, L., 1982. The earthquake cycle in subduction zones. Geophys. Res. Lett. 9, 21–24. https://doi.org/10.1029/GL009i001p00021.

Miyazaki, T., Sueyoshi, K., Hiraga, T., 2013. Olivine crystals align during diffusion creep of Earth's upper mantle. Nature 502, 321–326. https://doi.org/10.1038/nature12570.

Mompiou, F., Caillard, D., Legros, M., 2009. Grain boundary shear–migration coupling—I. In situ TEM straining experiments in Al polycrystals. J. Acta Mater. Res. 116, 2198–2209. https://doi.org/10.1016/j.actamat.2009.01.014.

Montagner, J.P., Kennett, B., 1996. How to reconcile body-wave and normal-mode reference Earth models. Geophys. J. Int. 125, 229–248. https://doi.org/10.1111/j.1365-246X.1996.tb06548.x.

Moresi, L., Solomatov, V., 1998. Mantle convection with a brittle lithosphere: thoughts on the global tectonic styles of the Earth and Venus. Geophys. J. Int. 133, 669–682. https://doi.org/10.1046/j.1365-246X.1998.00521.x.

Müller, R.D., Sdrolias, M., Gaina, C., Roest, W.R., 2008. Age, spreading rates, and spreading asymmetry of the world's ocean crust. Geochem. Geophys. Geosyst. 9, Q04006. https://doi.org/10.1029/2007GC001743.

Neves, S.P., Tommasi, A., Vauchez, A., Hassani, R., 2008. Intraplate continental deformation: influence of a heat-producing layer in the lithospheric mantle. Earth Planet. Sci. Lett. 274, 392–400. https://doi.org/10.1016/j.epsl.2008.07.040.

Paulson, A., Richards, M.A., 2009. On the resolution of radial viscosity structure in modelling long-wavelength postglacial rebound data. Geophys. J. Int. 179, 1516–1526.

Ricard, Y., Vigny, C., 1989. Mantle dynamics with induced plate tectonics. J. Geophys. Res., Solid Earth 94, 17543–17559. https://doi.org/10.1111/j.1365-246X.2009.04362.x.

Ritterbex, S., Carrez, P., Cordier, P., 2016. Modeling dislocation glide and lattice friction in Mg2SiO4 wadsleyite in conditions of the Earth's transition zone. Am. Mineral. 101, 2085–2094. https://doi.org/10.2138/am-2016-5578CCBYNCND.

Schmalholz, S.M., Duretz, T., Hetenyi, G., Medvedev, S., 2019. Distribution and magnitude of stress due to lateral variation of gravitational potential energy between Indian lowland and Tibetan plateau. Geophys. J. Int. 216, 1313–1333. https://doi.org/10.1093/gji/ggy463.

Schmalholz, S.M., Fletcher, R.C., 2011. The exponential flow law applied to necking and folding of a ductile layer. Geophys. J. Int. 184, 83–89. https://doi.org/10.1111/j.1365-246X.2010.04846.x.

Stotz, I.L., Iaffaldano, G., Davies, D.R., 2018. Pressure-driven Poiseuille flow: a major component of the torque-balance governing Pacific Plate motion. Geophys. Res. Lett. 45, 117–125. https://doi.org/10.1002/2017GL075697.

Tackley, P.J., 1996. Effects of strongly variable viscosity on three-dimensional compressible convection in planetary mantles. J. Geophys. Res. 101, 3311–3332. https://doi.org/10.1029/95JB03211.

Thieme, M., Demouchy, S., Mainprice, D., Barou, F., Cordier, P., 2018. Stress evolution and associated microstructure during transient creep of olivine at 1000–1200°C. Phys. Earth Planet. Inter. 278, 34–46. https://doi.org/10.1016/j.pepi.2018.03.002.

Thoraval, C., Tommasi, A., Doin, M.P., 2006. Plume-lithosphere interaction beneath a fast moving plate. Geophys. Res. Lett. 33. https://doi.org/10.1029/2005GL024047.

Tommasi, A., Mainprice, D., Canova, G., Chastel, Y., 2000. Viscoplastic self-consistent and equilibrium-based modeling of olivine lattice preferred orientations: implications for the upper mantle seismic anisotropy. J. Geophys. Res., Solid Earth 105, 7893–7908. https://doi.org/10.1029/1999JB900411.

Watts, A.B., 2001. Isostasy and Flexure of the Lithosphere. Cambridge University Press. https://doi.org/10.1017/S0016756802216696.

Wheeler, J., 2009. The preservation of seismic anisotropy in the Earth's mantle during diffusion creep. Geophys. J. Int. 178, 1723–1732. https://doi.org/10.1111/j.1365-246X.2009.04241.x.

Wilson, C., 2009. Modelling Multiple-Material Flows on Adaptive Unstructured Meshes. Ph.D. Thesis. Imperial College, London. https://doi.org/10.25560/5526.